ROYAL SOCIETY
OF CHEMISTRY

COMMUNICATION

Check for updates

A water-soluble fluorinated metal–organic cage based on paramagnetic copper as an efficient ^{1}H and ^{19}F MRI nanoprobe

Xin Fang, [a,b] Hongyu Yang, [b,c] Meina Liu, [ID] *[a] Xinyuan Zhu, [ID] [b] Xin Jin [ID] *[b] and Youfu Wang [ID] *[b]

Magnetic resonance imaging (MRI) is a critical clinical diagnostic tool, but conventional ^{1}H MRI suffers from background signal interference. ^{19}F MRI offers a promising alternative with near-zero background noise, yet its progress depends on high-performance fluorinated probes. Existing probes often struggle to balance fluorine content, water solubility, and relaxation efficiency. To address this issue, we developed a metal–organic cage (MOC) as a platform for a novel dual-modal MRI nanoprobe. Using copper ions as paramagnetic nodes and fluorinated oligoethylene glycol as ligands, we synthesized a structurally precise and water-soluble nanoprobe, MOC-F. This nanoprobe not only significantly enhances the ^{1}H relaxation rate through its paramagnetic copper centers, enabling high-contrast ^{1}H MRI (r_1 = 25.96 mM^{-1} s^{-1} at 298 K, 0.5 T), but also promotes an increased relaxation rate for ^{19}F nuclei *via* paramagnetic relaxation enhancement (a T_2/T_1 ratio of 0.86 at 500 MHz), thereby facilitating efficient ^{19}F MRI. Both *in vitro* and *in vivo* studies confirmed the outstanding dual-modal imaging performance and good biocompatibility of MOC-F. This work not only presents an innovative design strategy for developing highly sensitive ^{19}F MRI probes but also highlights the considerable potential of MOCs in biomedical imaging, opening new avenues for the development of advanced smart MRI nanoprobes.

1. Introduction

Magnetic resonance imaging (MRI) is an exceptionally powerful non-invasive imaging technique that utilizes the phenomenon of nuclear magnetic resonance to generate high-resolution, detailed images of internal anatomical structures within living organisms.[1,2] Due to the absence of ionizing radiation, MRI has

[a] School of Chemical and Environmental Engineering, Shanghai Institute of Technology, Shanghai 201418, P. R. China. E-mail: meina.liu@sit.edu.cn
[b] School of Chemistry and Chemical Engineering, State Key Laboratory of Polyolefins and Catalysis, Shanghai Jiao Tong University, Shanghai 200240, P. R. China. E-mail: jxcindy@sjtu.edu.cn, wyfown@sjtu.edu.cn
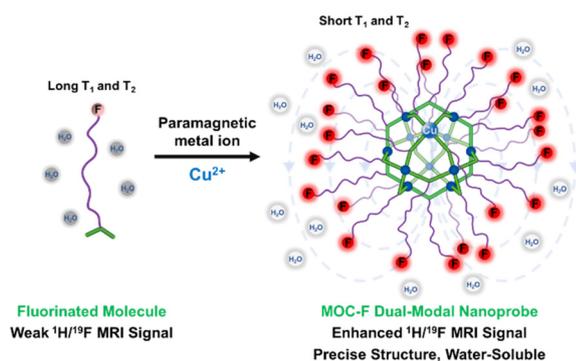*[c] School of Pharmacy, China Medical University, Shenyang 110122, P. R. China*

long been widely adopted in clinical diagnostics and biomedical research.[3,4] The most common form, ^{1}H MRI, first realized by Lauterbur in 1973,[5] detects variations in the relaxation times of ^{1}H signals (primarily from water molecules) across different tissues, thereby revealing detailed anatomical and pathological information. However, background signal interference caused by the excessively high natural abundance of ^{1}H in biological systems has become a critical limiting factor.[6–12] ^{19}F MRI, first reported in 1977, offers a compelling complement.[13] As the second most sensitive stable nuclide for MRI, ^{19}F possesses 100% natural abundance, a gyromagnetic ratio reaching 94% of ^{1}H, and virtually no endogenous background signal in soft tissues.[14–16] Critically, ^{1}H and ^{19}F MRI can share the same hardware, enabling multimodal imaging with minimal technical and cost barriers.[17–20] Meanwhile, it is important to emphasize that ^{19}F MRI does not replace anatomical ^{1}H MRI but rather complements it.[21,22] With near-zero background noise, ^{19}F MRI generates highly specific hotspot signals.[23] When these signals are overlaid onto ^{1}H images, they provide independent molecular information, thus enabling seamless integration of structure and function.[24,25]

Unlike ^{1}H MRI, the performance of ^{19}F MRI depends critically on the use of exogenous fluorinated contrast agents. Existing ^{19}F MRI probes are primarily categorized into five types—perfluorocarbons (PFCs), small fluorinated molecules (SFMs), fluorinated ionic liquids (FILs), fluorinated polymers, and inorganic fluoride nanoparticles (IFNPs)—each facing inherent trade-offs among fluorine content, water solubility, and relaxation efficiency.[26] PFCs offer high fluorine content but suffer from spectral complexity and hydrophobicity requiring encapsulation.[27] SFMs enable modular design, yet are limited by low fluorine content.[28–31] FILs combine solubility with high fluorine content but exhibit rapid clearance and limited chemical diversity.[32,33] Fluorinated polymers balance hydrophilicity and fluorine loading at the expense of chain rigidity and dispersibility,[34–38] while IFNPs, despite their high fluorine density, demand specialized UTE sequences due to extremely short T_2 relaxation.[39] Collectively, existing ^{19}F MRI probes are limited by trade-offs among sensitivity, design flexi-

bility, water solubility, and imaging compatibility.[40,41] There is a clear and urgent need for a new generation of ^{19}F probes that combine high fluorine content, excellent biocompatibility, and good water solubility with the capacity for precise molecular-level design and regulation.

Recent advances in supramolecular chemistry, particularly metal–organic cages (MOCs), have opened new avenues for probe design.[42] MOCs are discrete, precise nanostructures with tunable cavities formed via coordination-driven self-assembly.[43–45] Their structural symmetry, functional versatility,

Scheme 1 Structurally precise and water-soluble MOC-F nanoprobe with an enhanced ^{1}H/^{19}F dual-modal MRI signal.

and porosity enable diverse biomedical applications, yet current MOC-based imaging is largely limited to fluorescence, PET, and ^{1}H MRI.[46–48] Extending MOCs to emerging modalities therefore represents a promising frontier.

In response to current challenges and opportunities, we propose a MOC-based platform for constructing a novel ^{1}H/^{19}F dual-modal MRI probe. Using paramagnetic Cu^{2+} nodes[49] and fluorinated oligoethylene glycol-modified isophthalic acid ligands, we assembled a water-soluble, structurally precise cuboctahedral nanoprobe (MOC-F) via coordination-driven self-assembly. This system preserves the structural advantages of MOCs while enabling synergistic enhancement of both ^{1}H and ^{19}F MR signals, as shown in Scheme 1. By integrating structural precision with functional tunability, MOC-F provides a versatile and efficient nanoplatform for high-contrast biological imaging and structure–performance research.

2. Results and discussion

2.1 Synthesis and structural characterization

We first synthesized the fluorinated ligand L-F through a series of chemical reactions and then assembled it with copper ions via a self-assembly process to form the nanoscale cage, MOC-F. The detailed synthetic route and structural characterization data are shown in Fig. 1a and b and the SI
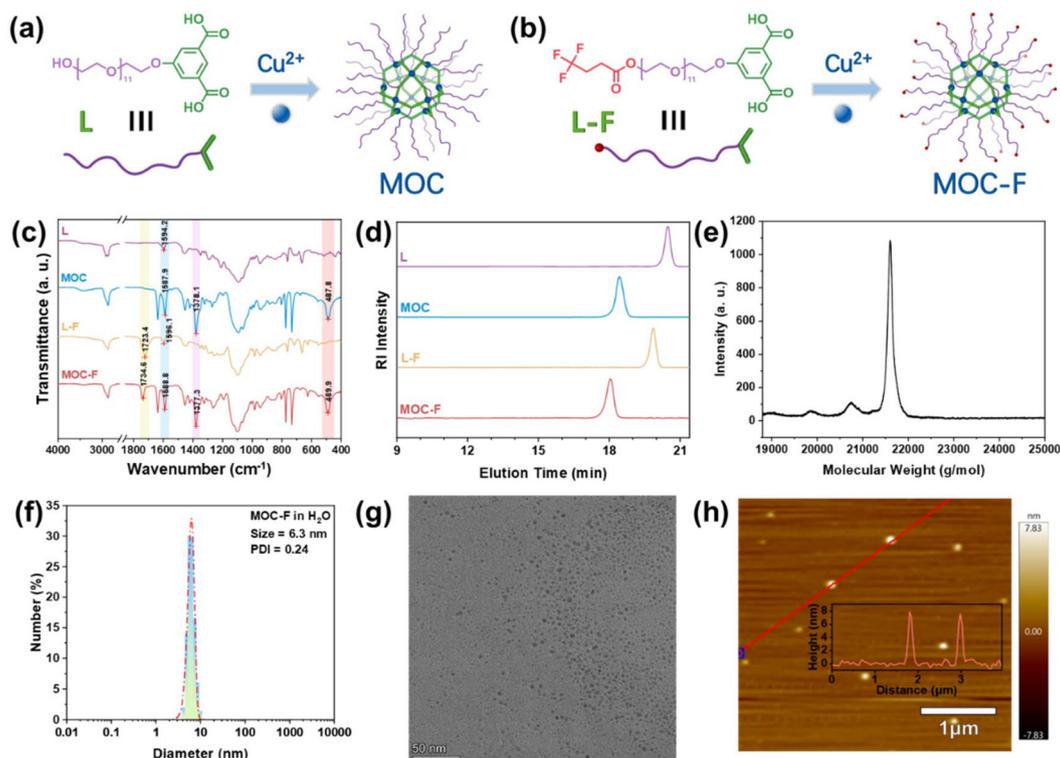

Fig. 1 Structural characterization of MOCs. (a and b) Chemical structures of the organic ligands and corresponding MOCs. (c) FT-IR spectra demonstrating characteristic functional group changes. (d) SEC profiles comparing the hydrodynamic volumes of two ligands, MOC and MOC-F. (e) MALDI-TOF mass spectrum confirming the molecular weight of MOC-F. (f) DLS measurement of MOC-F in water, indicating its hydrodynamic diameter distribution. (g) TEM image of MOC-F (scale bar: 50 nm). (h) AFM image (scale bar: 1 μm) and corresponding height analysis of MOC-F.

(Scheme S1 and Fig. S1–S14). To facilitate a systematic comparison of their structures and properties, we simultaneously synthesized the reference compound L without fluorine and its corresponding nanoscale cage, MOC. Analysis of the ^{1}H NMR spectra of L, MOC, L-F, and MOC-F revealed that most chemical shift signals in MOC and MOC-F exhibited significant broadening and downfield shifts compared to their corresponding ligands (Fig. S15 and S16). This phenomenon indicates coordination interactions between the ligands and Cu^{2+}, consistent with the coordination-induced chemical shift trends reported in previous literature.[50–52] Specifically, the proton signals attributed to the aromatic ring in L and L-F (8.18 and 7.70 ppm, and 8.20 and 7.73 ppm, respectively) merged, broadened, and shifted to 7.38 ppm (MOC) and 7.43 ppm (MOC-F) upon cage formation. Additionally, the ^{19}F NMR spectrum of MOC-F exhibits a single signal at −66.96 ppm (Fig. S17), further confirming the presence of only one fluorine chemical environment in its structure, consistent with our molecular design expectations for this probe.

Fourier transform infrared (FT-IR) spectroscopy provided crucial evidence for successful coordination and fluorine source introduction. As shown in Fig. 1c, both L-F and MOC-F exhibit characteristic absorption peaks at 1723.4 cm^{-1} and 1734.6 cm^{-1} originating from the ester carbonyl group in the fluorinated structure, while this signal is completely absent in L or MOC, clearly demonstrating the successful introduction of the fluorine source. Furthermore, the characteristic stretching vibrations of the carboxyl group in ligands L and L-F occur at 1594.2 cm^{-1} and 1596.1 cm^{-1}, respectively. Following the formation of the cage structure, MOC exhibits two sets of absorption bands at 1587.9 cm^{-1} and 1378.1 cm^{-1}, while MOC-F shows two sets at 1588.8 cm^{-1} and 1377.3 cm^{-1}. These are attributed to the stretching vibrations of the carboxylate ions, indicating coordination between the carboxyl group and the copper ion. Notably, both MOC and MOC-F exhibit characteristic Cu–O bond peaks at 487.8 cm^{-1} and 489.9 cm^{-1}, respectively, providing further corroboration for the formation of the coordination structure.

Based on the confirmed molecular structure and the established tendency for isophthalic acid and copper ions to form coordination bonds within the $Cu_{24}L_{24}$ cuboctahedral skeleton, coupled with the high molecular weight characteristics of the ligands and MOCs, we systematically investigated the molecular weight, stability, homogeneity, and polydispersity of the assembly via size exclusion chromatography (SEC). Fig. 1d shows a single sharp peak for L and L-F at approximately 20.48 and 19.86 min, while peaks for MOC and MOC-F appeared at 18.43 and 18.05 min, respectively. The shorter elution times of MOC and MOC-F reflect their larger hydrodynamic volumes compared to the respective ligands. The molecular weights of MOC and MOC-F determined by SEC were 10 857 and 17 832 g mol^{-1}, respectively, approximately matching the theoretical values. Additionally, all four samples exhibited extremely narrow polydispersity indices of 1.07, 1.06, 1.05, and 1.04, respectively, indicating low dispersity and structural stability. We further measured the molecular weight of MOC-F via

matrix-assisted laser desorption/ionization time-of-flight (MALDI-TOF) mass spectrometry, observing a peak at 21 537 g mol^{-1} consistent with the theoretical value, thereby confirming the formation of the structurally expected MOC-F (Fig. 1e). Based on the molecular formula, each MOC-F contains 72 fluorine atoms residing in identical chemical environments, corresponding to a fluorine content of approximately 6.36 wt%. Detailed information regarding the comparative samples L-F and MOC is presented in Table S1.

Benefiting from the oligoethylene glycol (OEG) linkages between the fluorine moiety and the MOC core, MOC-F exhibits exceptional water solubility, reaching up to 50 mg mL^{-1}. For subsequent bioapplication experiments, we employed dynamic light scattering (DLS) and zeta potential measurements to determine the size and surface charge of MOC-F. The results indicate that MOC-F exhibits a hydrated particle size of approximately 6.3 nm with a uniform distribution (PDI = 0.24) (Fig. 1f), carries a weak negative surface charge (−5.5 mV) (Fig. S18), and remains stable for 12 hours. To further evaluate its stability in physiological environments, we dissolved MOC-F in PBS buffer (pH 7.4) or fetal bovine serum (FBS) and retested after two days (Fig. S19). The DLS results showed that its size remained consistent with the aforementioned values, confirming the good structural integrity and stability under simulated physiological conditions. Finally, we visually characterized the nanoscale morphology of MOC-F using transmission electron microscopy (TEM) and atomic force microscopy (AFM). TEM imaging showed that MOC-F possesses a nearly spherical morphology with a uniform, ultrasmall size of approximately 7 nm (Fig. 1g). A representative AFM image (Fig. 1h) clearly reveals that the synthesized MOC-F consists of discrete, uniformly distributed nanoparticles. The average height of these particles was determined to be approximately 7.5 nm. These data align closely with the theoretical dimensions of $Cu_{24}L_{24}$ cuboctahedral MOC, not only experimentally confirming its successful synthesis and structural integrity but also providing crucial evidence for its excellent structural stability and narrow size distribution.

2.2 Evaluation of imaging performance

Following comprehensive characterization of MOC-F, its atomically precise structure and ultra-small size and features prompted us to explore its potential as a ^{19}F MRI contrast agent. The quality of MRI can be represented by the signal-to-noise ratio (SNR). It is well known that the SNR exhibits a negative correlation with the longitudinal relaxation time T_1; more precisely, the SNR is proportional to $\sqrt{1/T_1}$. However, during MRI signal acquisition, the SNR is also influenced by the transverse relaxation time T_2. Specifically, the average signal amplitude (S_{avg}) obtained per acquisition, and consequently the overall SNR, is positively correlated with T_2, i.e., SNR $\propto e^{-1/T_2}$.[53] Research has demonstrated that introducing chemical reagents to accelerate relaxation processes can simultaneously shorten both T_1 and T_2, though the extent of shortening may not be consistent between the two. If T_2 is excessively shortened, the resulting decrease in S_{avg} may outweigh

the gain from increasing the number of average repetitions (NEX), leading to signal "quenching". Conversely, if T_2 is moderately reduced and the increase in NEX compensates for the loss in S_{avg}, signal enhancement may be achieved. Generally, a T_2/T_1 ratio greater than 0.4 is considered a practical criterion for effective relaxation sensitization.[54] Paramagnetic metal ions are frequently employed as contrast enhancers, with copper ions exhibiting particularly strong paramagnetic properties. This constitutes one rationale for selecting copper as the metallic node within the MOC structure in this study. We hypothesise that the copper ion at the MOC centre modulates the relaxation times of surrounding ^1H nuclei of water molecules and the ^{19}F nuclei at the MOC periphery through interactions with both the inner and outer spheres. This synergistically enhances $^1H/^{19}F$ magnetic resonance signals (Fig. 2a). To preliminarily evaluate the effect of Cu^{2+} on ^{19}F relaxation, we compared the ^{19}F NMR spectra of the L-F (without Cu^{2+}) and the assembled MOC-F (with Cu^{2+}). As anticipated, the ^{19}F NMR spectrum of MOC-F exhibits a marked broadening of the chemical shift lines, confirming that the potential interaction between the Cu^{2+} ion and the ^{19}F nucleus results in accelerated relaxation (Fig. 2b).

Therefore, we investigated the performance of L-F, MOC, and MOC-F as potential ^1H MRI contrast agents at 0.5 T. We first measured the relaxation times of the three samples at different concentrations. As shown in Table S2, the T_1 and T_2 of the ^1H nuclei in L-F are in the thousands of milliseconds range, while the T_1 and T_2 of the ^1H nuclei in both MOC samples are shortened to varying degrees. The shortened T_1 and T_2 of ^1H in both MOC and MOC-F are attributed to the presence of paramagnetic Cu^{2+} within MOCs. With increasing sample concentration, the ^1H T_1 and T_2 of MOC and MOC-F samples shortened significantly, while those of the L-F sample showed no noticeable change (Fig. S20). Simultaneously, the introduction of the paramagnetic metal ion Cu^{2+} into the probe consistently maintained the T_2/T_1 ratio within an appropriate range (>0.66), confirming the successful sensitization of this probe class. Since this probe exhibits a marked shortening of longitudinal relaxation time due to the presence of Cu^{2+}, which maintains the T_2/T_1 ratio within an optimal range to enhance the SNR, it can be classified as a T_1-weighted probe. Plotting the reciprocal of the relaxation time *versus* concen-

tration yields longitudinal and transverse relaxation efficiencies of 26.13 and 33.68 $mM^{-1} s^{-1}$ for MOC, respectively, while MOC-F exhibits longitudinal and transverse relaxation efficiencies of 25.96 and 34.18 $mM^{-1} s^{-1}$, respectively, markedly higher than those of L-F (Fig. 3a). These results indicate that the ^1H nuclear relaxation processes in both MOC samples are significantly accelerated. This acceleration stems from the pronounced paramagnetic relaxation enhancement (PRE) effect imparted by the paramagnetic Cu^{2+} ions. This effect also lays the foundation for enhancing the SNR and image quality in MRI using such probes.

Based on the above results, we further conducted *in vitro* ^1H MRI imaging experiments on aqueous samples of L-F, MOC, and MOC-F to visually evaluate their imaging performance. As shown in Fig. 3b, the imaging results clearly demonstrate that both MOCs (MOC and MOC-F) produce MRI with a high SNR and uniform signal distribution. Their signal intensity exhibits significant dependence on probe concentration—with a regular increase in signal intensity as the probe concentration increases. This phenomenon aligns with typical relaxation-enhanced mechanisms, further confirming the crucial role of paramagnetic components in enhancing imaging contrast. In contrast, under identical imaging conditions, the L-F aqueous solution without paramagnetic metals produced only an extremely weak signal, with imaging performance significantly inferior to MOC and MOC-F. This intergroup discrepancy powerfully demonstrates that the paramagnetic centers provided by Cu^{2+} ions in the structure are the fundamental cause of effective MRI signal generation. The significant relaxation enhancement effect they induce not only substantially increases imaging sensitivity but also enables MOC and MOC-F to exhibit outstanding signal response characteristics in aqueous environments, thereby revealing their immense potential as high-performance ^1H MRI probes.

Fig. 3 The relationship between relaxation rates and the concentrations of related probes for ^1H (a) and ^{19}F (c). The ^1H (b) and ^{19}F (d) MR images of related probes at different concentrations (concentration [C] refers to the molar concentration of the probe molecule (MOC, L-F, or MOC-F). Fluorine atom concentration [F] is calculated from [C]. For MOC-F, each molecule contains 72 equivalent ^{19}F atoms, and thus [F] = 72 × [C]. For L-F, each molecule contains 3 fluorine atoms, and thus [F] = 3 × [C]).
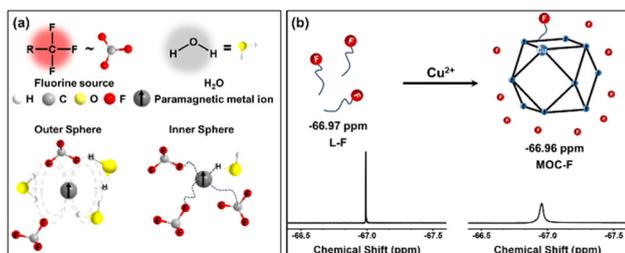

Fig. 2 (a) Relaxation modulation of paramagnetic ions on fluorinated moieties and water molecules. (b) ^{19}F NMR spectra of the free L-F ligand and hinged L-F on MOC-F containing Cu^{2+} ions.
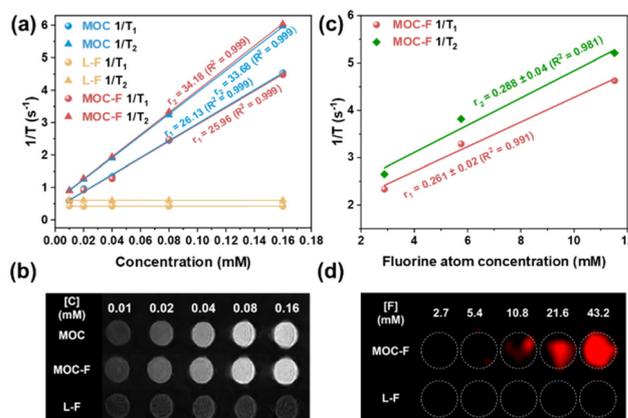
Similarly, to investigate the feasibility of MOC-F for ^{19}F MRI, we compared the ^{19}F nuclear relaxation behavior of L-F and MOC-F. The results indicate that both ^{19}F nuclear T_1 and T_2 of MOC-F in aqueous solution decrease significantly with increasing concentration (Fig. S21), with a T_2/T_1 ratio exceeding 0.86 (Table S3 and Fig. S22–24). This classification confirms its status as a T_1-weighted ^{19}F MRI probe. In contrast, the relaxation times of L-F exhibit no apparent concentration dependence. Furthermore, quantitative calculations revealed longitudinal and transverse relaxation efficiencies of 0.261 and 0.288 mM^{-1} s^{-1} for MOC-F, respectively (Fig. 3c). Compared to the ligand (Fig. S22 and Table S4), these relaxation efficiencies exhibited an order-of-magnitude enhancement, highlighting the crucial role of metal coordination in boosting fluorine nuclear relaxation efficiencies.

During *in vitro* ^{19}F MR imaging experiments, we conducted comparative studies using fluorine atom concentration as the standard. Since MOC-F contains 72 fluorine atoms and L-F contains 3 fluorine atoms, the molecular concentration of L-F is three times that of MOC-F at the same fluorine atom concentration. *In vitro* ^{19}F MRI imaging results further confirmed the critical role of the metal center; in the control group without Cu^{2+}, no significant ^{19}F MRI signal was detected in the L-F solution (Fig. 3d). In contrast, at the same fluorine atom concentration, MOC-F exhibited significantly enhanced imaging performance, with signal intensity increasing regularly with the sample concentration gradient, demonstrating clear concentration dependence. Based on this dose–response relationship, the detection limit of MOC-F for ^{19}F nuclei under the experimental conditions was determined to be below 10.8 mM. These results conclusively demonstrate that MOC-F is a high-performance ^{19}F MRI contrast agent. Combined with the previously described ^{1}H MRI imaging performance, it is confirmed that MOC-F successfully achieves ^{1}H/^{19}F dual-modal MRI *in vitro* experiments. Furthermore, this nanoprobe exhibits excellent water solubility and high relaxation efficiency. These characteristics collectively provide a solid foundation for its further application in biomedical imaging.

To further evaluate the MRI performance of this nanoprobe in biological systems, *in vivo* imaging experiments were conducted in mice. All animal procedures were performed in accordance with the Guide for the Care and Use of Laboratory Animals (National Institutes of Health, USA) and were approved by the Animal Ethics Committee of Shanghai Jiao Tong University (No. 202601056). Prior to *in vivo* experiments, the cellular biocompatibility of both MOC and MOC-F was evaluated. The methylthiazol-2-yl-tetrazolium (MTT) assay demonstrated that HK-2 cells essentially maintained a viability rate exceeding 80% after 24 h of incubation, even at high probe concentrations, indicating negligible cytotoxicity (Fig. 4a). To assess potential long-term cytotoxicity, we continuously monitored HK-2 cell viability at 36 or 48 h post-probe treatment *via* MTT assay. The results showed that HK-2 viability remained consistently around 80% (Fig. S25), indicating no significant long-term toxicity from the probe. To evaluate the probe's labeling efficiency and cellular uptake rate, we
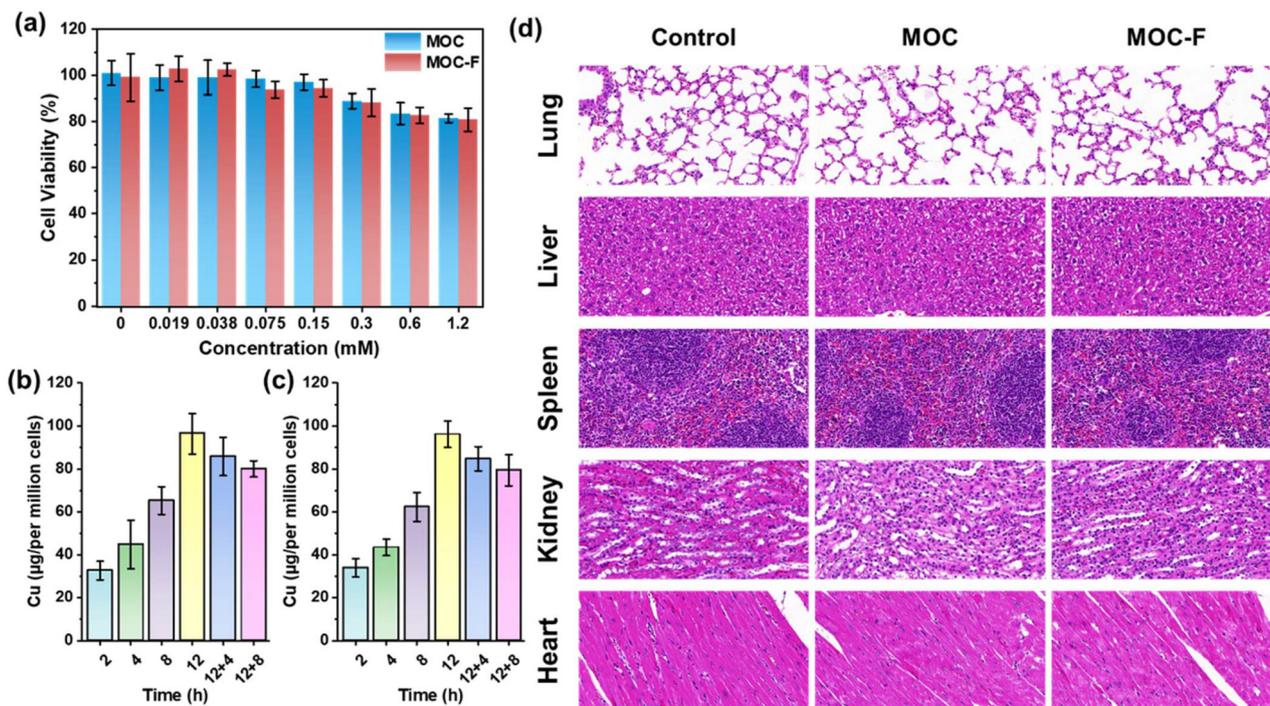

Fig. 4 (a) The impact of MOC (the concentration range is 0–1.2 mM, corresponding to 0–22.2 mg mL^{-1}.) and MOC-F (the concentration range is 0–1.2 mM, corresponding to 0–25.8 mg mL^{-1}) on HK-2 cell viability assessed using the MTT assay. Cellular uptake of MOC (b) and MOC-F (c) in HK-2 cells. (d) The evaluation of the biocompatibility of MOC and MOC-F through H&E staining of major organs.

quantitatively measured intracellular copper content using inductively coupled plasma optical emission spectroscopy (ICP-OES) to determine cellular uptake of MOC and MOC-F. The results showed a linear increase in probe uptake over time until removal at 12 hours, followed by a gradual decline in concentration (Fig. 4b and c). For MOC-F, each cell contained approximately 2.7×10^{12} ^{19}F nuclei after 12 h incubation, and this level remained at 2.3×10^{12} ^{19}F nuclei per cell 8 hours after the medium replacement. This indicates sufficiently prolonged intracellular retention of the probe, which is crucial for future MRI-based long-term *in vivo* cell tracking. To evaluate the biocompatibility of MOC and MOC-F in the major mouse organs including lung, liver, spleen, kidneys, and heart, mice received intravenous injections of MOC or MOC-F solutions (the concentration of MOC is 1.2 mM, corresponding to 22.2 mg mL^{-1}, and the concentration of MOC-F is also 1.2 mM, corresponding to 25.8 mg mL^{-1}), with samples collected two days post-injection. Tissue sections were examined after hematoxylin and eosin (H&E) staining. As shown in Fig. 4d, all organs in the three groups exhibited structurally uniform histomorphology without obvious damage. This multi-level experimental evidence, ranging from *in vitro* cells to *in vivo* tissues, collectively supports the excellent biosafety of MOC and MOC-F probes under the described experimental protocols, thereby enabling subsequent *in vivo* imaging studies.

To systematically evaluate the *in vivo* imaging efficacy of the developed nanoprobe, we conducted MRI experiments using a C57BL/6 mouse model. A 200 μL PBS solution of the MOC-F probe (1.2 mM, equivalent to 25.8 mg mL^{-1}, corresponding to 86.4 mM ^{19}F) was subcutaneously injected into the right hindlimb of the mice, while the left hindlimb received 200 μL PBS solution of MOC (1.2 mM, equivalent to 22.2 mg mL^{-1}) as the control group (Fig. 5a). Subsequently, ^{1}H and ^{19}F MRI scans

were performed. The results demonstrated significant ^{1}H MRI signal enhancement at both injection sites, indicating that the probe effectively enhances water proton relaxation *in vivo*. Furthermore, only the MOC-F-injected right hindlimb exhibited an intense ^{19}F MRI signal (Fig. 5b), confirming MOC-F retains ^{19}F imaging capability within living tissue. These findings confirm the success of our research strategy: Cu^{2+} simultaneously modulates ^{1}H and ^{19}F relaxation processes to enhance dual-modal MRI signals. Moreover, the MOC-F probe demonstrates excellent imaging performance *in vivo*, combining high ^{1}H MRI resolution with high ^{19}F MRI specificity. Furthermore, the probe exhibits good biocompatibility and stability *in vivo*, with sufficient signal intensity for clear imaging.

3. Conclusions

This study successfully developed a dual-modality ^{1}H/^{19}F MRI probe, MOC-F, based on a metal–organic cage (MOC) featuring an atomically precise structure. MOC-F integrates 72 equivalent fluorine atoms within a single water-soluble cuboctahedral framework, achieving a fluorine content of 6.36 wt%. By harnessing the inherent paramagnetism of its Cu^{2+} nodes, MOC-F exhibits high longitudinal relaxivities for ^{1}H ($r_1 = 25.96$ mM^{-1} s^{-1}) and ^{19}F ($r_1 = 0.261$ mM^{-1} s^{-1}) at 0.5 T, along with an excellent T_2/T_1 ratio (>0.86), enabling efficient T_1-weighted imaging for both nuclei. This achievement underscores the unique value of supramolecular assembly strategies in constructing high-performance imaging probes—retaining the precise controllability of small molecules while incorporating the exceptional properties of nanomaterials. Compared to conventional ^{19}F MRI probes, MOC-F successfully overcomes the inherent trade-offs present in existing platforms. Unlike perfluorocarbon-based probes that require encapsulation and often exhibit complex multi-peak spectra, MOC-F possesses excellent water solubility and provides a single ^{19}F NMR signal. In contrast to fluorinated polymers and inorganic nanoparticles that typically lack intrinsic ^{1}H MRI capability or require specialized sequences (*e.g.*, UTE), MOC-F offers inherent synergistic dual-mode contrast. Its well-defined architecture further enables accurate structure–property correlations. As shown in SI Table S5, while MOC-F does not surpass all previous studies on any single metric, it achieves an optimal balance across multiple key performance parameters, validating its potential as a next-generation ^{19}F probe platform.

The successful development of MOC-F not only provides a novel strategy to overcome the sensitivity limitations of conventional ^{19}F MRI probes but also highlights the immense potential of metal–organic cages in biomedical applications. Its excellent compatibility with clinical MRI equipment lays a solid foundation for practical translation. Looking ahead, this study pioneers a new pathway for precisely regulating nanoprobe performance and investigating structure–property relationships through supramolecular design. Leveraging the
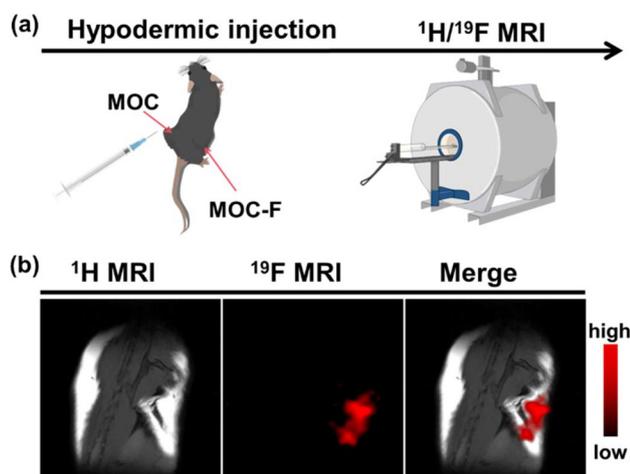

Fig. 5 *In vivo* imaging using MOC and MOC-F probes. (a) Schematic of dual-modality imaging experiments. (b) ^{1}H, ^{19}F, and fused magnetic resonance imaging spectra corresponding to injected mice after subcutaneous injection of 200 μL 1.2 mM MOC (22.2 mg mL^{-1}) and 200 μL 1.2 mM MOC-F (25.8 mg mL^{-1}, corresponding to 86.4 mM ^{19}F) into designated sites.

platform's modularity, targeted functionality can be introduced by modifying the organic ligands—for instance, conjugating peptides or small molecules (such as RGD peptides or folate) to the cage periphery without disrupting its core architecture. Alternatively, biotin–streptavidin interactions or click chemistry can be employed to link antibodies or aptamers, enabling active targeting of specific disease biomarkers. Further optimization of the probe's targeting capabilities and pharmacokinetic properties holds promise for significant contributions to precision disease diagnosis and therapeutic monitoring, ultimately accelerating the clinical translation of imaging probes.

Author contributions

X. Fang: investigation, methodology, and writing – original draft. H. Yang: methodology and formal analysis. X. Zhu: validation and investigation. M. Liu, X. Jin, and Y. Wang: funding acquisition, supervision and writing – review & editing.

Conflicts of interest

There are no conflicts to declare.

Data availability

All data generated or analysed during this study are available from the corresponding author on reasonable request. The SI includes synthetic details and structural characterizations of related compounds. It also provided supplemental MRI performance of related compounds. See DOI: https://doi.org/10.1039/d6nr00177g.

Acknowledgements

References

1 D. H. Lysak, K. Downey, L. S. Cahill, W. Bermel and A. J. Simpson, *Nat. Rev. Methods Primers*, 2023, **3**, 91.

2 M. E. Tiryaki, P. Esmaeili-dokht, J. Lazovic, K. P. Pruessmann and M. Sitti, *Nat. Commun.*, 2025, **16**, 10840.

3 J. Stender, O. Gosseries, M.-A. Bruno, V. Charland-Verville, A. Vanhaudenhuyse, A. Demertzi, C. Chatelle, M. Thonnard, A. Thibaut, L. Heine, A. Soddu, M. Boly, C. Schnakers, A. Gjedde and S. Laureys, *Lancet*, 2014, **384**, 514–522.

4 W. Zhao, C. Li, J. Chang, H. Zhou, D. Wang, J. Sun, T. Liu, H. Peng, Q. Wang, Y. Li and A. K. Whittaker, *Prog. Polym. Sci.*, 2023, **146**, 101739.

5 P. C. Lauterbur, *Nature*, 1973, **242**, 190–191.

6 C. Zhang, B. Nan, J. Xu, T. Yang, L. Xu, C. Lu, X.-B. Zhang, J. Rao and G. Song, *Nat. Biomed. Eng.*, 2024, **9**, 671–685.

7 J. Hu, C. Wang, D. Yao and D. Wang, *Coord. Chem. Rev.*, 2025, **537**, 216709.

8 C. Zhang, L. Xu, B. Nan, C. Lu, H. Liu, L. Lei, R. Yue, G. Guan, M. He, X.-B. Zhang and G. Song, *ACS Nano*, 2023, **17**, 9529–9542.

9 W. Yang, C. Deng, X. Shi, Y. Xu, C. Dai, H. Wang, K. Bian, T. Cui and B. Zhang, *ACS Nano*, 2023, **17**, 4009–4022.

10 J. Salaam, T. Fogeron, G. Pilet, R. Bolbos, C. Bucher, L. Khrouz and J. Hasserodt, *Angew. Chem., Int. Ed.*, 2022, **62**, e202212782.

11 E. A. Kras, E. M. Snyder, G. E. Sokolow and J. R. Morrow, *Acc. Chem. Res.*, 2022, **55**, 1435–1444.

12 S. Anbu, S. H. L. Hoffmann, F. Carniato, L. Kenning, T. W. Price, T. J. Prior, M. Botta, A. F. Martins and G. J. Stasiuk, *Angew. Chem.*, 2021, **133**, 10831–10839.

13 G. N. Holland, P. A. Bottomley and W. S. Hinshaw, *J. Magn. Reson.*, 1977, **28**, 133–136.

14 F. Liu, X. Li, Y. Li, S. Xu, C. Guo and L. Wang, *Chem. Sci.*, 2024, **15**, 17397–17406.

15 X. Tang, A. Li, C. Zuo, X. Liu, X. Luo, L. Chen, L. Li, H. Lin and J. Gao, *ACS Nano*, 2023, **17**, 5014–5024.

16 H. Zhou, M. Qi, J. Shao, X. Li, Z. Zhou, S. Yang and H. Yang, *J. Magn. Magn. Mater.*, 2021, **518**, 167436.

17 Z. Jin, P. Yue, F. Chen, Q. Chen, G. Angelovski and G. Wang, *Inorg. Chem. Commun.*, 2025, **178**, 114518.

18 D. Wang, S. Yan, J. Sun, X. Xia, Z. Pan, Z. Liu, Q. Wang, Y. Li and W. Zhao, *ACS Macro Lett.*, 2024, **13**, 1286–1292.

19 Z. Garda, F. Szeremeta, O. Quin, E. Molnar, B. Varadi, R. Clemencon, S. Meme, C. Pichon, G. Tircso and E. Toth, *Angew. Chem., Int. Ed.*, 2024, **63**, e202410998.

20 U. Flogel, S. Temme, C. Jacoby, T. Oerther, P. Keul, V. Flocke, X. Wang, F. Bonner, F. Nienhaus, K. Peter, J. Schrader, M. Grandoch, M. Kelm and B. Levkau, *Nat. Commun.*, 2021, **12**, 5847.

21 X. Tang, X. Gong, J. Ming, D. Chen, H. Lin and J. Gao, *Anal. Chem.*, 2020, **92**, 16293–16300.

22 R. Pujales-Paradela, T. Savic, D. Esteban-Gomez, G. Angelovski, F. Carniato, M. Botta and C. Platas-Iglesias, *Chemistry*, 2019, **25**, 4782–4792.

23 S. Temme, P. Kleimann, Z. B. Tiren, P. Bouvain, A. Zielinski, W. Dollmeyer, S. Poth, J. Gorges and U. Flogel, *Int. J. Mol. Sci.*, 2025, **26**, 2462.

24 Y. Zhu, L. Zhang, S. Li, Y. Luo, L. Xiao, Q. Yu, Z. X. Jiang, X. Zhou and S. Chen, *Anal. Chem.*, 2025, **97**, 9265–9275.

25 G. Yu, W. Yang, Y. Wang, X. Zhou and B. Zhang, *Coord. Chem. Rev.*, 2025, **542**, 216860.

26 Y. Jiang, X. Luo, L. Chen, H. Lin and J. Gao, *Fundam. Res.*, 2023, **3**, 529–533.

27 K. Akazawa, F. Sugihara, T. Nakamura, H. Matsushita, H. Mukai, R. Akimoto, M. Minoshima, S. Mizukami and K. Kikuchi, *Angew. Chem., Int. Ed.*, 2018, **57**, 16742–16747.

28 L. Li, A. Li, J. Wang, J. Shao, H. Zhou, Z. Peng, H. Lin and J. Gao, *Biomaterials*, 2025, **317**, 123073.

29 Z. Chai, Q. Wu, K. Cheng, X. Liu, Z. Zhang, L. Jiang, X. Zhou, M. Liu and C. Li, *Angew. Chem., Int. Ed.*, 2023, **62**, e202300318.

30 A. Li, X. Luo, D. Chen, L. Li, H. Lin and J. Gao, *Anal. Chem.*, 2023, **95**, 70–82.

31 L. Li, C. Chen, Y. Bu, J. Wang, J. Shao, A. Li, H. Lin and J. Gao, *Anal. Chem.*, 2024, **96**, 10827–10834.

32 L. Chen, Y. Jiang, N. Xiong, Y. Fan, H. Lin and J. Gao, *ACS Nano*, 2025, **19**, 9061–9069.

33 X. Zhu, H. Xiong, S. Wang, Y. Li, J. Chi, X. Wang, T. Li, Q. Zhou, J. Gao and S. Shi, *Adv. Healthc. Mater.*, 2022, **11**, e2102079.

34 T. A. T. Arin and O. Sedlacek, *Biomacromolecules*, 2024, **25**, 5630–5649.

35 J. Chang, H. Zhou, C. Li, J. Sun, Q. Wang, Y. Li and W. Zhao, *Biomacromolecules*, 2023, **24**, 2918–2927.

36 C. Li, H. Zhou, J. Sun, D. Wang, J. Chang, Q. Wang, Y. Li and W. Zhao, *Biomacromolecules*, 2023, **24**, 2777–2789.

37 V. M. Panakkal, D. Havlicek, E. Pavlova, M. Filipova, S. Bener, D. Jirak and O. Sedlacek, *Biomacromolecules*, 2022, **23**, 4814–4824.

38 T. A. T. Arin, D. Havlicek, D. F. D. Daza, N. Jirat-Ziolkowska, O. Pop-Georgievski, D. Jirak and O. Sedlacek, *Mater. Today Bio.*, 2025, **31**, 101462.

39 D. Cohen, O. Brontvein and A. Bar-Shir, *ACS Appl. Nano Mater.*, 2024, **7**, 6791–6796.

40 C. Zhang, K. Yan, C. Fu, H. Peng, C. J. Hawker and A. K. Whittaker, *Chem. Rev.*, 2022, **122**, 167–208.

41 I. Tirotta, V. Dichiarante, C. Pigliacelli, G. Cavallo, G. Terraneo, F. B. Bombelli, P. Metrangolo and G. Resnati, *Chem. Rev.*, 2015, **115**, 1106–1129.

42 Y. Wang, Y. Zhang, X. Duan, J. Mao, M. Pan, J. Shen and C. Su, *Coord. Chem. Rev.*, 2024, **501**, 215570.

43 C. Huang, Y. Deng, R. Ma, H. Ge, F. Gong, J. Yang, X. Zhu and Y. Wang, *Nanoscale*, 2024, **16**, 9406–9411.

44 D. Sun, Y. Deng, J. Dong, X. Zhu, J. Yang and Y. Wang, *Chem. Eng. J.*, 2024, **497**, 154648.

45 P. Yin, D. Sun, Y. Deng, X. Zhu, Y. Wang, J. Yang and X. Feng, *Theranostics*, 2024, **14**, 4861–4873.

46 Y. Fan, D. Chen, L. Chen, K. Liu, Y. Zheng, L. Li, J. Li, H. Lin and J. Gao, *Nano Lett.*, 2023, **23**, 11989–11998.

47 Y. Fan, X. Chi, J. Li, Y. Zheng, L. Chen, Y. Jiang, Z. Yin, H. Lin and J. Gao, *Nano Today*, 2024, **57**, 102364.

48 S. M. McLeod, L. Robison, G. Parigi, A. Olszewski, R. J. Drout, X. Gong, T. Islamoglu, C. Luchinat, O. K. Farha and T. J. Meade, *ACS Appl. Mater. Interfaces*, 2020, **12**, 41157–41166.

49 K. P. Malikidogo, H. Martin and C. S. Bonnet, *Pharmaceuticals*, 2020, **13**, 436.

50 C. Huang, Z. Liu, Y. Deng, X. Wang, Q. Miao, D. Sun, X. Zhu, J. Yang and Y. Wang, *Theranostics*, 2025, **15**, 2564–2578.

51 C. Huang, J. Li, X. Zhu and Y. Wang, *Nanoscale*, 2023, **15**, 19475–19479.

52 Y. Deng, X. Fang, Y. Lv, X. Zhu, Y. Wang, X. Wang and X. Feng, *Mater. Horiz.*, 2026, **13**, 786–799.

53 H. Lin, X. Tang, A. Li and J. Gao, *Adv. Mater.*, 2021, **33**, e2005657.

54 U. Flogel and E. Ahrens, *Fluorine Magnetic Resonance Imaging*, Jenny Stanford Publishing, New York, 2016.